



Cite this: *RSC Adv.*, 2024, **14**, 1962

## High-sensitivity hybrid MoSe<sub>2</sub>/AgInGaS quantum dot heterojunction photodetector<sup>†</sup>

Xunjia Zhao,<sup>‡,a</sup> Xusheng Wang,<sup>‡,a</sup> Runmeng Jia,<sup>a</sup> Yuhai Lin,<sup>a</sup> TingTing Guo,<sup>a</sup> Linxiang Wu,<sup>a</sup> Xudong Hu,<sup>‡,a</sup> Tong Zhao,<sup>a</sup> Danni Yan,<sup>a</sup> Lin zhu,<sup>b</sup> Zhanyang Chen,<sup>b</sup> Xinsen Xu,<sup>b</sup> Xiang Chen<sup>‡,a\*</sup> and Xiufeng Song<sup>‡,a\*</sup>

Zero-dimensional (0D)–two-dimensional (2D) hybrid photodetectors have received widespread attention due to their outstanding photoelectric performances. However, these devices with high performances mainly employ quantum dots that contain toxic elements as sensitizing layers, which restricts their practical applications. In this work, we used eco-friendly AgInGaS quantum dots (AIGS-QDs) as a highly light-absorbing layer and molybdenum diselenide (MoSe<sub>2</sub>) as a charge transfer layer to construct a 0D–2D hybrid photodetector. Notably, we observed that MoSe<sub>2</sub> strongly quenches the photoluminescence (PL) of AIGS-QDs and decreases the decay time of PL in the MoSe<sub>2</sub>/AIGS-QDs heterojunction. The MoSe<sub>2</sub>/AIGS-QDs hybrid photodetector demonstrates a responsivity of  $14.3 \text{ A W}^{-1}$  and a high detectivity of  $6.4 \times 10^{11} \text{ Jones}$ . Moreover, the detectivity of the hybrid phototransistor is significantly enhanced by more than three times compared with that of the MoSe<sub>2</sub> photodetector. Our work suggests that 0D–2D hybrid photodetectors with multiplex I–III–VI QDs provide promising potential for future high-sensitivity photodetectors.

Received 24th October 2023  
 Accepted 4th January 2024

DOI: 10.1039/d3ra07240a  
[rsc.li/rsc-advances](http://rsc.li/rsc-advances)

### 1. Introduction

In recent decades, graphene, being a representative 2D material, has gained significant attention due to its exceptionally high carrier mobility ( $2 \times 10^5 \text{ cm}^2 \text{ V}^{-1} \text{ s}^{-1}$ ), wide range of optical absorption coefficients ( $7 \times 10^5 \text{ cm}^{-1}$ ), and excellent photoelectric conversion efficiency.<sup>1–3</sup> These properties make it highly attractive for the development of high-speed and broadband photodetectors.<sup>4,5</sup> Nonetheless, the semi-metallic property with low light absorptivity of only 2.3% results in the large dark current and low photoelectric response of graphene-based devices.<sup>6</sup> This problem restricts the practical application of graphene in the field of photodetectors.<sup>7</sup>

Hence, it is necessary to explore a new technology strategy with high light absorptivity to address this limitation. A commonly employed approach to enhance device performance is to integrate graphene with a high light absorption QDs.<sup>8</sup> QDs have some exceptional properties with high light absorption coefficient, a wide range of adjustable bandgap, and a narrow linewidth in emission.<sup>9–11</sup> Therefore, QDs have attracted extensive attention and applied in various fields such as

photodetectors, solar cells, and LEDs. Konstantatos *et al.* demonstrated a hybrid graphene–quantum dot phototransistor with a gain of  $\sim 10^8$  electrons per photon and a responsivity of  $\sim 10^7 \text{ A W}^{-1}$ .<sup>12,13</sup> Hu *et al.* reported a graphene/InAs QDs/GaAs photodetector that has a responsivity of about  $17.0 \text{ mA W}^{-1}$  and detectivity of  $2.3 \times 10^{10} \text{ Jones}$ .<sup>14</sup> Zheng *et al.* revealed that the photoconductive gain and detectivity of graphene-perovskite quantum dot photodetector arrive at  $3.7 \times 10^4$  and  $6 \times 10^7 \text{ Jones}$ .<sup>15</sup>

Besides, the zero-band gap of graphene leads to the ultra-fast carrier recombination speed and ultra-short carrier lifetime.<sup>16</sup> The graphene photodetectors do not satisfy the requirements of high-response optoelectronic devices due to the large dark current.<sup>17</sup> Hence, two-dimensional transition metal dichalcogenide (2D TMDC) semiconductors exhibit appealing properties, such as tunable bandgaps, high electron mobility, flexibility, and the absence of dangling bonds on their surfaces.<sup>18–23</sup> These characteristics enable 2D TMDCs to be an excellent candidate for the high-performance photodetector.<sup>24–26</sup> In recent years, numerous 0D/2D heterostructures with outstanding properties have been explored and reported. For instance, Zhang *et al.* explored that the detectivity of MoS<sub>2</sub>/ZnCdSe heterostructure is reached to be  $1.0 \times 10^{12} \text{ Jones}$ .<sup>27</sup> Hu *et al.* reported that the responsivity and detectivity of WSe<sub>2</sub>/PbS-QDs heterostructure are  $2 \times 10^5 \text{ A W}^{-1}$  and  $10^{13} \text{ Jones}$ , respectively.<sup>28</sup> Mukherjee *et al.* found that the detectivity of MoS<sub>2</sub>/PbS-QDs heterostructure reaches up to  $10^{12} \text{ Jones}$ .<sup>29</sup> Among these, PbS-QDs,<sup>30</sup> HgTe-QDs,<sup>31</sup> and CdS-QDs<sup>32</sup> are

<sup>a</sup>MIIT Key Laboratory of Advanced Display Materials and Devices, School of Materials Science and Engineering, Nanjing University of Science and Technology, Nanjing 210094, China. E-mail: xiangchen@njust.edu.cn; xiufengsong@njust.edu.cn

<sup>b</sup>Shandong Gemei Tungsten & Molybdenum Material Co. Ltd, Weihai 265222, China

† Electronic supplementary information (ESI) available. See DOI: <https://doi.org/10.1039/d3ra07240a>

‡ These authors contributed equally to this work.



commonly employed in the development of high-performance photodetectors. However, these devices face a challenge due to the presence of high-toxicity elements which limit their practical application.<sup>4</sup> Hence, it is essential to explore alternative eco-friendly QDs possessing comparable characteristics in the photodetectors. So, low-toxicity QDs with a wide emission spectrum, tunable bandgap energy ranging from visible to near-infrared, and large Stokes shifts have emerged as promising alternatives to cadmium and lead-based QDs.<sup>33,34</sup>

Here, we introduced a strategy to take advantages of high light absorption and eco-friendly I-III-VI QDs with the high carrier mobility characteristic of 2D materials, which can significantly enhance photoresponsivity and detectivity. The 0D/2D heterojunction integrated MoSe<sub>2</sub> and AIGS-QDs can effectively facilitate the separation of electron and hole pairs with charge transfer at the interface, leading to the enhancement of the photoelectric performance. The responsivity and detectivity of the hybrid MoSe<sub>2</sub>/AIGS-QDs photodetector exhibit a high responsivity of  $14.3 \text{ A W}^{-1}$  and a large detectivity of  $6.4 \times 10^{11} \text{ Jones}$ , which is three times higher than those of the MoSe<sub>2</sub> device. These results indicate that the utilization of hybrid MoSe<sub>2</sub>/AIGS-QDs heterostructures in photodetectors holds significant promise for achieving high-performance detection capabilities.

## 2. Experimental section

### 2.1 Synthesis of the MoSe<sub>2</sub>

MoSe<sub>2</sub> films were synthesized using a two-step process involving magnetron sputtering and a selenization process. First, the SiO<sub>2</sub>/Si substrate was ultrasonicated sequentially in ethanol, acetone, and deionized water. Afterward, an open window of  $20 \mu\text{m} \times 100 \mu\text{m}$  or  $50 \mu\text{m} \times 50 \mu\text{m}$  was formed by photolithography method. Then, the 8 nm Mo film was deposited on SiO<sub>2</sub>/Si substrate by the magnetron sputtering using a Mo target at a power of 30 W and a pressure of  $2 \times 10^{-3} \text{ Torr}$ . The MoSe<sub>2</sub> film was fabricated by selenylation method in a thermal furnace (Fig. S1†). The SiO<sub>2</sub>/Si substrate with Mo film was positioned in the center zone of a quartz tube. 500 mg Se powder was placed upstream of 18 cm away from the SiO<sub>2</sub>/Si substrate. The quartz tube was then evacuated and argon gas was introduced to remove the residual oxygen in the tube and restore atmospheric pressure. During the reaction, the argon flow rate was maintained at 120 sccm. The substrate temperature was raised to 850 °C for 60 minutes and then maintained at 850 °C for 120 minutes. Additionally, hydrogen was introduced at a flow rate of 30 sccm for 3 hours. The temperature of the Se powder zone is initially set at 50 °C for the first 30 minutes, followed by a gradual increase to 400 °C over the next 30 minutes. It is then maintained at 400 °C for 120 minutes. Subsequently, the furnace was cooled naturally to room temperature.

### 2.2 Synthesis of the AIGS-QDs

For the synthesis of AIGS-QDs, a three-neck flask was charged with 0.2 mmol of AgNO<sub>3</sub>, 0.4 mmol of indium acetate (In(Ac)<sub>3</sub>), and 0.6 mmol of gallium acetylacetone (Ga(Ac)<sub>3</sub>). Following

this, a solution was prepared by injecting 2 ml of 1-dodecanethiol (DDT), 2 ml of oleylamine (OAm), and 5 ml of 1-octadecene (1-ODE) into the mixture while applying magnetic stirring. The solution was subjected to two rounds of vacuuming and nitrogen charging, followed by heating at a temperature of 50 °C for a duration of thirty minutes. Additionally, the solution was subjected to heating at a temperature of 90 °C. Subsequently, the S precursor (consisting of 1.6 mmol of sulphur dissolved in 2.5 ml of 1-ODE) was introduced into the solution. Pure AgInGaS cores can be obtained by iteratively performing precipitation and dispersion using hexane and ethanol. AIGS cores were collected to facilitate subsequent device fabrication.<sup>35</sup>

### 2.3 Device fabrication

Electrode pattern was prepared by standard electron beam lithography (EBL) and the 3 nm Cr and 60 nm Au were deposited as electrical contacts on MoSe<sub>2</sub> layer by electron-beam evaporation (EBE). After that, prepared AIGS-QDs were spin-coated MoSe<sub>2</sub> layer with 2500 rpm for 30 s to obtain a heterojunction device.

### 2.4 Characterization

The crystal structure and morphology of the AIGS-QDs and MoSe<sub>2</sub> were measured by an X-ray diffractometer (Bruker Advanced D8), atomic force microscopy (AFM) (Bruker Multi-mode 8), an optical microscope (OM) (Olympus BX51) and transmission electron microscopy (FEI, TECNAIG2 20 LaB6). The composition and binding energy of AIGS-QDs and MoSe<sub>2</sub> were determined using X-ray photoelectron spectroscopy (XPS) with the PHI QUANTERA II instrument. The optical spectra were obtained by UV-vis-IR (Shimadzu, UV3600), PL and Raman spectroscopy (Horiba, HR EVO NANO) and time-resolved PL decay transients (Horiba FLTCSPC). UPS was measured using He I lines (Thermo ESCALAB 250XI). All optoelectronic characterizations were performed using Semiconductor Device Analyzer (Keysight B1500A) at room temperature and ambient conditions. The examination of the photoelectric response properties was conducted using semiconductor lasers (MDL-III442/100 mW) with a wavelength of 442 nm. The light intensity was detected with an optical power meter (Newport PMKIT-21-01).

## 3. Results and discussion

The crystal structure of the MoSe<sub>2</sub>/AIGS-QDs heterojunctions is presented in Fig. 1a. The AIGS-QDs solution illuminated under UV radiation (365 nm) appears orange. In order to confirm the crystal structure of AIGS-QDs, the XRD pattern for AIGS-QDs (Ag : Ga = 2 : 3) is presented in Fig. S2.† The diffraction peaks of AIGS-QDs located at 27.5°, 46.8°, and 54.7°, corresponding to the (112), (105), and (303) crystal plane of tetragonal AgInS<sub>2</sub> (PDF# 25-1328) and AgGaS<sub>2</sub> (PDF# 73-1233). The obtained results demonstrate the successful preparation of the AIGS-QDs.<sup>36,37</sup> To evaluate AIGS-QDs quality, the transmission electron microscope (TEM) and high-resolution transmission



electron microscope (HRTEM) was utilized to analyze the microstructure and atomic arrangement, as shown in Fig. S3† and 1b. The TEM image and the histograms of the AIGS-QDs size distribution indicate homogeneous dispersing and the mean diameter of sphere-shaped AIGS-QDs is 2.43 nm. The particle size is mainly distributed between 2.1 and 2.7 with a narrow size distribution (Fig. S3b†). The HRTEM image exhibits continuous lattice fringes. This means that the AIGS-QDs have clear crystal structures and the interplanar spacing is 0.32 nm, which is consist with the (112) lattice plane of AIGS-QDs.<sup>38</sup>

X-ray photoemission spectroscopy (XPS) is employed to identify the elemental composition and electron binding energy in AIGS-QDs. The XPS analysis of AIGS-QDs is presented in Fig. S4,† which reveals the presence of four major elements. There are two peaks observed at 371 eV and 365 eV, which can be attributed to the Ag 3d<sub>3/2</sub> and Ag 3d<sub>5/2</sub> orbitals, respectively. The 3d spectra of indium (In) exhibit two prominent peaks located at 449.5 eV and 441.9 eV, which align with the

distinctive In 3d<sub>3/2</sub> and In 3d<sub>5/2</sub> orbitals, respectively. The peaks observed at 1141.8 eV and 1114.8 eV correspond to the Ga 2p<sub>1/2</sub> and Ga 2p<sub>3/2</sub> orbitals, respectively. In addition, the S 2p<sub>1/2</sub> and S 2p<sub>3/2</sub> orbitals exhibit energies of approximately 160 eV and 158.7 eV, respectively. All of these results are in accord with the previous reports of AIGS-QDs.<sup>34,39</sup>

The MoSe<sub>2</sub> was grown by the selenylation method using Se power precursors and Mo film. To confirm the MoSe<sub>2</sub> thin film quality, Atomic Force Microscope (AFM), XPS and Raman images were gained. The thickness of MoSe<sub>2</sub> was verified at about 15 nm by AFM (Fig. 1c), which shows smooth surfaces of the samples and is similar to previous report.<sup>40,41</sup> The optical microscope (OM) photograph of a square MoSe<sub>2</sub> film displayed in Fig. S5† appears uniform color. XPS measurements were introduced to further characterize the MoSe<sub>2</sub> film. The elements of Mo, Se, O and C can be identified in Fig. S6.† XPS spectra of the two primary elements of Mo and Se in the MoSe<sub>2</sub> film are presented in Fig. 1d. The two peaks at 229.3 eV and 232.4 eV correspond to the Mo 3d<sub>5/2</sub> and 3d<sub>3/2</sub> orbitals. Similarly, the 3d

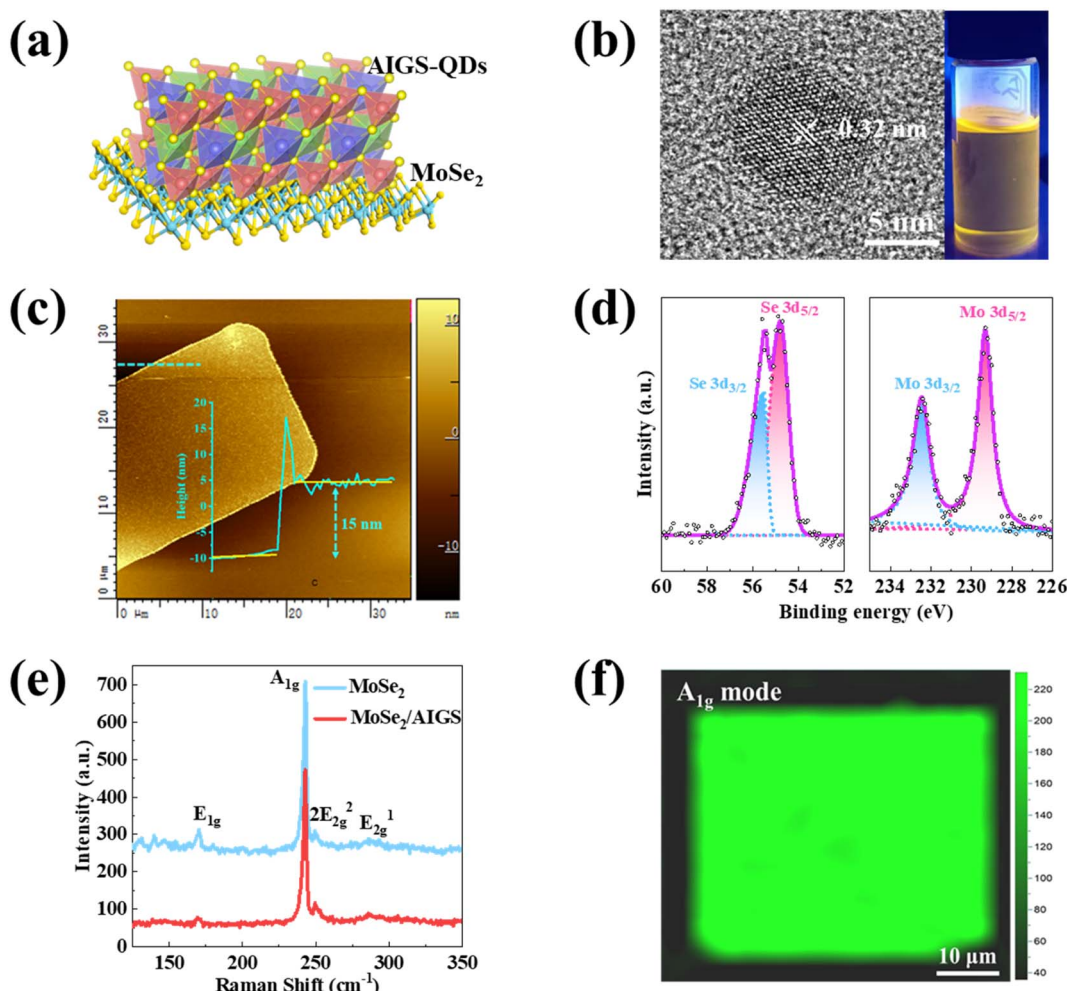
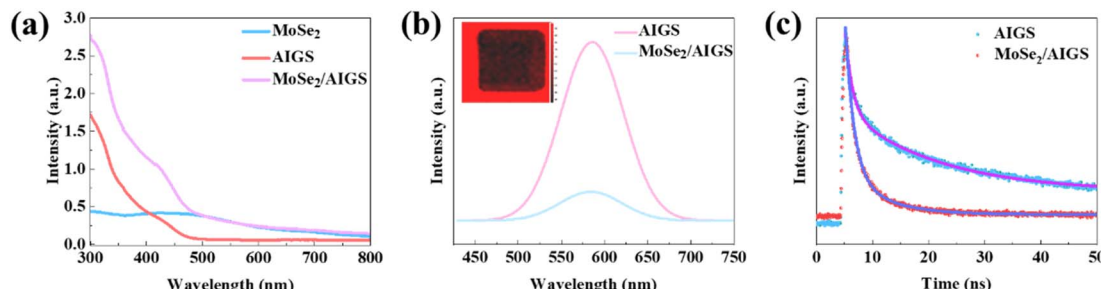


Fig. 1 Characteristics of AIGS-QDs, MoSe<sub>2</sub>, and MoSe<sub>2</sub>/AIGS-QDs heterojunctions. (a) Schematic representation of the crystal structure of the MoSe<sub>2</sub>/AIGS-QDs heterojunction. (b) HRTEM image of AIGS-QDs. Inset: photograph of the AIGS-QDs solution under UV radiation (365 nm). (c) AFM image of the MoSe<sub>2</sub>. Inset: the thickness of MoSe<sub>2</sub>. (d) XPS of Mo and Se. (e) Raman spectra of MoSe<sub>2</sub> and MoSe<sub>2</sub>/AIGS-QDs heterojunctions. (f) Raman mapping of MoSe<sub>2</sub> (A<sub>1g</sub> mode).





**Fig. 2** Optical properties of the MoSe<sub>2</sub> and MoSe<sub>2</sub>/AIGS-QDs heterojunction. (a) UV-vis absorption spectra of the MoSe<sub>2</sub>, AIGS-QDs, and MoSe<sub>2</sub>/AIGS-QDs. (b) PL spectra of AIGS-QDs and MoSe<sub>2</sub>/AIGS-QDs. Inset: the PL mapping of the MoSe<sub>2</sub> that was covered with AIGS-QDs (the red zone is only AIGS-QDs and the dark zone is MoSe<sub>2</sub> coupling with AIGS-QDs). (c) TRPL decay transients measured at 570 nm for AIGS-QDs and MoSe<sub>2</sub>/AIGS-QDs.

spectra of Se show two major peaks located at 54.8 eV and 55.5 eV, consistent with the characteristic Se 3d<sub>5/2</sub> and 3d<sub>3/2</sub> orbitals, respectively, which are in agreement with the previous work.<sup>42,43</sup>

The Raman spectra of MoSe<sub>2</sub> and MoSe<sub>2</sub>/AIGS-QDs were excited under 532 nm and presented in Fig. 1e to provide additional insights into the structure and composition of MoSe<sub>2</sub>. The MoSe<sub>2</sub> sample presents a dominant Raman peak at approximately 242.0 cm<sup>-1</sup>, which corresponds to an out-of-plane Raman mode known as the A<sub>1g</sub> mode. Three additional peaks are observed at approximately 169.1 cm<sup>-1</sup>, 249.6 cm<sup>-1</sup>, and 285.7 cm<sup>-1</sup>, respectively. These peaks correspond to the vibration modes of in-plane modes E<sub>1g</sub>, 2E<sub>2g</sub><sup>2</sup>, and E<sub>2g</sub><sup>1</sup>, which are consistent with previous research results.<sup>44,45</sup> The A<sub>1g</sub> mode of MoSe<sub>2</sub> flake exhibits the highest intensity due to the strong interlayer interaction. Meanwhile, a higher peak intensity of the A<sub>1g</sub> mode generally indicates a lower number of layers.<sup>45</sup> The

presence of a distinct peak in the sharp A<sub>1g</sub> mode confirms the high quality of the MoSe<sub>2</sub> sheeting. To comprehensively understand the quality of selenylation, a Raman mapping of MoSe<sub>2</sub> was collected around the A<sub>1g</sub> mode (242.0 cm<sup>-1</sup>), as displayed in Fig. 1f. It is noteworthy to mention that the uniform intensity observed across the whole area (50 μm × 50 μm) of the MoSe<sub>2</sub> thin film indicates the consistent thickness. Furthermore, when the AIGS-QDs were spun on the surface of MoSe<sub>2</sub> (Fig. S7†), no new peaks were observed, suggesting that the AIGS-QDs layer does not disrupt the structure of MoSe<sub>2</sub>.<sup>46</sup> Consequently, these results demonstrate the successful preparation of high-quality AIGS-QDs/MoSe<sub>2</sub> heterojunction, which can be used as the response materials in the photodetector.

To assess the optical properties of the MoSe<sub>2</sub>/AIGS-QDs heterojunction, the absorption spectrum, PL, PL mapping, and TRPL were recorded. The UV-vis absorption spectra of the pure AIGS-QDs, MoSe<sub>2</sub>, and hybrid MoSe<sub>2</sub>/AIGS-QDs samples

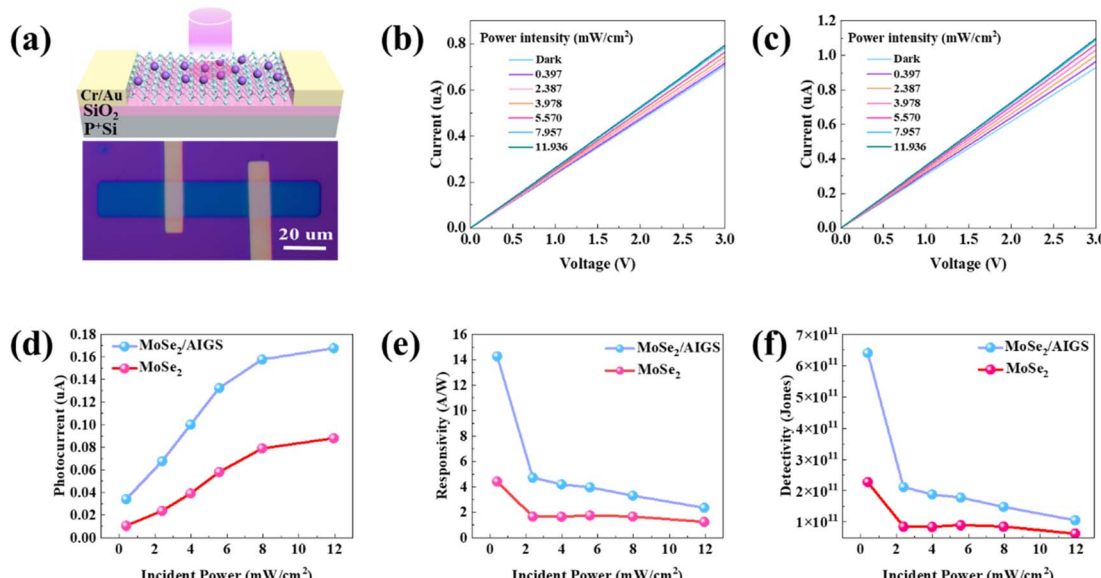


**Fig. 3** Photoelectric response characteristics of the MoSe<sub>2</sub> and MoSe<sub>2</sub>/AIGS-QDs heterojunction device under 442 nm illumination. (a) Schematic diagram and optical image of the hybrid photodetector. (b and c) Output current of the MoSe<sub>2</sub> and hybrid MoSe<sub>2</sub>/AIGS-QDs photodetector measured under different power intensities. (d-f) Photocurrent, responsivity and specific detectivity of the MoSe<sub>2</sub> and hybrid MoSe<sub>2</sub>/AIGS-QDs photodetector measured at  $V_{ds}$  = 3 V under different power intensities.

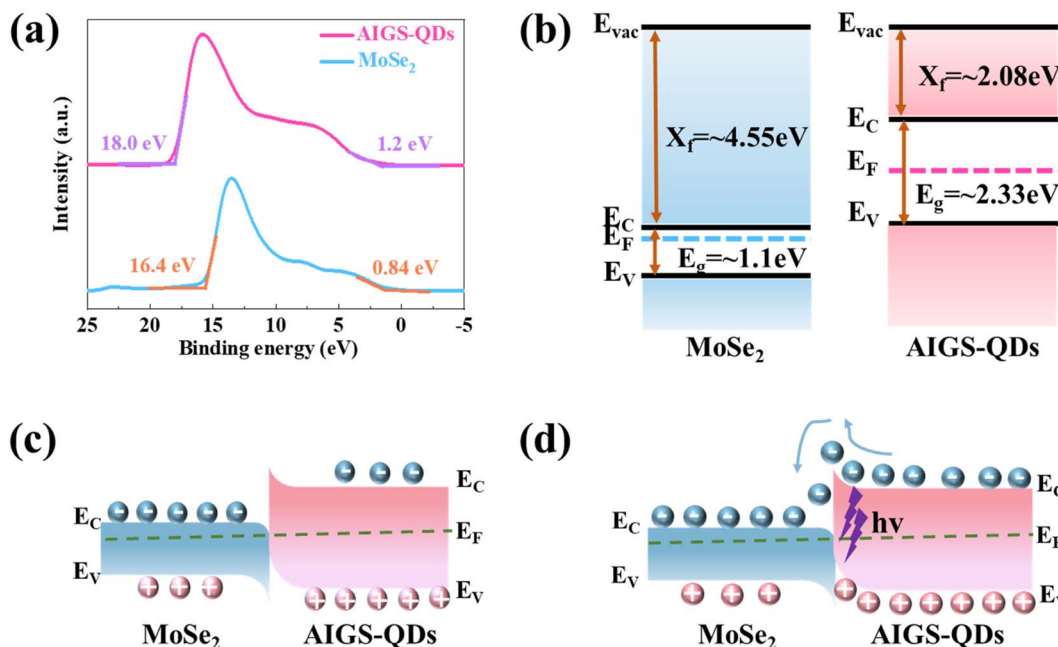


Fig. 4 Charge transfer mechanism. (a) Ultraviolet photoelectron spectroscopy (UPS) measurement results of AIGS-QDs and MoSe<sub>2</sub>. (b) Energy band diagram of MoSe<sub>2</sub> (left) and AIGS-QDs (right). (c and d) Mechanism of charge-carrier injection between AIGS-QDs and MoSe<sub>2</sub> in contact state under dark and contact state under illumination.

were measured, as depicted in Fig. 2a. The absorption spectrum of MoSe<sub>2</sub> displays a broad absorption range spanning from 300 to 800 nm. When the AIGS-QDs were coated on the MoSe<sub>2</sub> film, the MoSe<sub>2</sub> film exhibited a significantly enhanced absorption in the wavelength range of 300–480 nm, which is attributed to the cooperative absorption of AIGS-QDs and the MoSe<sub>2</sub> layers. This high absorption of the hybrid MoSe<sub>2</sub>/AIGS-QDs heterojunction indicates its potential for application in the field of photodetectors.<sup>47,48</sup>

The PL spectra of AIGS-QDs and MoSe<sub>2</sub>/AIGS-QDs heterostructure were obtained with photoexcitation at 3.8 eV (325 nm) and emerged in Fig. 2b. There is a peak around 577 nm in PL of pure AIGS-QDs. After being coupled with MoSe<sub>2</sub>, there exhibits a significant quenching of about 84% reduction compared with that of the pristine AIGS-QDs. This phenomenon explains that

a large number of photon-generated carriers may be transferred between AIGS-QDs and MoSe<sub>2</sub>.<sup>49</sup> The PL mapping was measured to further reveal the charge exchange between AIGS-QDs and MoSe<sub>2</sub>. As shown in the inset of Fig. 2b, the zone of QDs was bright (red color) but the zone of MoSe<sub>2</sub> was dark square, which illustrates that MoSe<sub>2</sub> has a strong quenching of PL on AIGS-QDs. This PL quenching is associated with the charge transfer at the interface of the AIGS-QDs and MoSe<sub>2</sub> heterojunction.<sup>50</sup>

To comprehensively elucidate the charge transfer dynamics occurring at the interfaces between MoSe<sub>2</sub> and AIGS-QDs, TRPL measurements were utilized. The TRPL decay curves in Fig. 2c were fitted using a biexponential decay equation to determine the lifetime of both AIGS-QDs and the MoSe<sub>2</sub>/AIGS-QDs heterostructure. The pristine AIGS-QDs exhibited a significantly long PL lifetime of 15.84 ns, indicating slow recombination of

Table 1 Performance comparison of the reported 2D–0D heterojunction photodetectors

	Layer thickness (nm)	Measurement condition	R (A W <sup>-1</sup> )	D* (Jones)	References
MoS <sub>2</sub> /PbS-QDs	8 nm	400–1600	0.6	10 <sup>12</sup>	29
WSe <sub>2</sub> /CdSe-QD	1.019 nm (CVD)	638	9.27	4.38 × 10 <sup>10</sup>	56
MoS <sub>2</sub> /ZnO-QDs	Monolayer (CVD)	405	0.084	1.05 × 10 <sup>11</sup>	57
Graphene/WS <sub>2</sub> QDs	Monolayer (CVD)	365	3.1 × 10 <sup>2</sup>	8.9 × 10 <sup>8</sup>	61
MoSe <sub>2</sub> /CsPb(Cl/Br) <sub>3</sub> -QDs	Few-layer	455	104	—	62
MoSe <sub>2</sub>	Few-layer	455	34	—	62
MoSe <sub>2</sub>	Monolayer	514	0.32	3.54 × 10 <sup>12</sup>	63
MoSe <sub>2</sub>	44 nm	785	238	7.6 × 10 <sup>11</sup>	64
MoS <sub>2</sub> /PbSe-QDs	4.02 nm	1310	137.6	7.7 × 10 <sup>10</sup>	65
<i>n</i> -WS <sub>2</sub> / <i>p</i> -PbS QDs	Multilayer	1550	0.18	4.11 × 10 <sup>11</sup>	66
MoSe <sub>2</sub>	15 nm	442	4.42	2.28 × 10 <sup>11</sup>	This work
MoSe <sub>2</sub> /AIGS-QDs	15 nm	442	14.3	6.4 × 10 <sup>11</sup>	This work



carriers in the AIGS-QDs. However, when coupled with  $\text{MoSe}_2$ , the lifetime ( $\tau$ ) decreases significantly from 15.84 to 4.46 ns, suggesting a substantial charge transfer occurring at the interface between AIGS-QDs and  $\text{MoSe}_2$ .<sup>48,51</sup> Under light illumination, photogenerated electrons exhibit a strong tendency to transfer from AIGS-QDs to  $\text{MoSe}_2$ , while the generated holes remain in AIGS-QDs, forming the separation of the electrons and holes. This charge transfer results in a reduced probability of recombination<sup>51</sup> and the accumulation of unpaired electrons and holes, leading to strong quenching and the shortened lifetime of the PL. Meanwhile, charge transfer is beneficial to the electrons and holes separation at the interface of the heterojunction, which is advantageous for enhancing the photocurrent. The strong optical absorption and effective charge transfer demonstrate that  $\text{MoSe}_2$ /AIGS-QDs heterojunction is a promising application in photodetector.

The schematic diagram and practical optical image of the  $\text{MoSe}_2$  and  $\text{MoSe}_2$ /AIGS-QDs photodetector device are depicted in Fig. 3a. To compare the photoelectric detection performance between  $\text{MoSe}_2$  devices with and without AIGS-QDs, the output curves were plotted in Fig. 3b and c. Both the  $I$ - $V$  curves of the  $\text{MoSe}_2$  and  $\text{MoSe}_2$ /AIGS-QDs heterostructure device are linear, which implies a good ohmic contact between Cr/Au electrodes and  $\text{MoSe}_2$  (or  $\text{MoSe}_2$ /AIGS-QDs). The dark current of the original and heterojunction devices is measured to be approximately 0.706  $\mu\text{A}$  and 0.931  $\mu\text{A}$ , respectively, at a source-drain voltage ( $V_{\text{ds}}$ ) of 3 V. Under light irradiation (illuminated by a 442 nm laser at 11.936  $\text{mW cm}^{-2}$ ), the output current of the  $\text{MoSe}_2$  heterojunction device increased from 0.706  $\mu\text{A}$  to 0.795  $\mu\text{A}$ , compared with that in the dark. After being coupled with AIGS-QDs, the output current of the hybrid device increases to 1.099  $\mu\text{A}$ . The photocurrents ( $I_{\text{ph}} = I_{\text{light}} - I_{\text{dark}}$ ) of the device were calculated in Fig. 3d. Both the photocurrents of the pure  $\text{MoSe}_2$  device and the hybrid device exhibit a monotonic increase with increasing optical power intensity. It is worth pointing out that after combining with QDs, the photocurrent is two times larger than that of the pristine  $\text{MoSe}_2$  photodetector. This phenomenon demonstrates that the integration of AIGS-QDs with  $\text{MoSe}_2$  leads to an increase in photocurrent in hybrid devices. These results suggest that the photosensitizing layer AIGS-QDs can effectively improve the performance of the  $\text{MoSe}_2$  photodetector.

To evaluate the device performance of the photocurrent in individual  $\text{MoSe}_2$  and heterojunction photodetector, two important indicators, namely responsivity ( $R$ ) and specific detectivity ( $D^*$ ), are introduced. These indicators play a crucial role in determining the performance of photodetectors.

The photoelectric conversion capability of the device, denoted as  $R$ , was evaluated with a wavelength of 442 nm under various incident power intensities at 3 V. The responsivity was calculated using the formula  $R = I_{\text{ph}}/PS$ ,<sup>52-54</sup> where  $I_{\text{ph}}$  represents the photocurrent,  $P$  denotes the incident power intensity, and  $S$  represents the area of the device channel with dimensions of 30  $\mu\text{m}$  length and 20  $\mu\text{m}$  width. As shown in Fig. 3e, there is a decrease in the responsivity of both devices as the incident power intensity increases. This trend may be attributed to the lower recombination probability of carriers at lower incident power intensity.<sup>55</sup> The highest responsivity was found at the

minimum incident power intensity (0.357  $\text{mW cm}^{-2}$ ) for the  $\text{MoSe}_2$  device is about 4.42  $\text{A W}^{-1}$ . Once the AIGS-QDs were coated on the  $\text{MoSe}_2$  surface, the responsivity was calculated to be 14.3  $\text{A W}^{-1}$ , which is improved more than three times compared to that of the  $\text{MoSe}_2$  photodetector. This value is at a higher level compared with those in previous work, such as  $\text{MoS}_2$ / $\text{PbS}$ -QDs (0.6  $\text{A W}^{-1}$ ),<sup>29</sup>  $\text{WSe}_2$ / $\text{CdSe}$ -QD (9.27  $\text{A W}^{-1}$ ),<sup>56</sup> and  $\text{MoS}_2$ / $\text{ZnO}$ -QDs (0.084  $\text{A W}^{-1}$ ).<sup>57</sup> These results demonstrate our hybrid 2D/QDs device presents a potential replacement for toxic hybrid photodetectors with excellent performance.

In addition, the  $D^*$  is another crucial parameter for assessing the capability of signal detection in the presence of noise. It is defined as  $D^* = RS^{1/2}/(2eI_{\text{dark}})^{1/2}$ , where  $S$  represents the effective detection area of the device,  $e$  denotes the electronic charge, and  $I_{\text{dark}}$  corresponds to the dark current, as illustrated in Fig. 3f.<sup>58,59</sup> Similar to  $R$ , the maximum value of  $D^*$  for the device is observed at the minimum light power. After being deposited with the AIGS-QDs layer, the  $D^*$  value of the heterojunction device increases three times compared to that of the  $\text{MoSe}_2$  device (from  $2.28 \times 10^{11}$  Jones to  $6.4 \times 10^{11}$  Jones). Furthermore, the  $D^*$  value of the  $\text{MoSe}_2$ /AIGS-QDs device is superior to those of previously reported 2D/0D photodetectors. For instance, the  $D^*$  value of  $\text{WSe}_2$ / $\text{CdSe}$ -QD was reported to be  $4.38 \times 10^{10}$  Jones,<sup>56</sup>  $\text{MoS}_2$ / $\text{PbS}$ -QDs had a  $D^*$  value of  $1 \times 10^{11}$  Jones,<sup>60</sup> and graphene/ $\text{WS}_2$ -QDs exhibited a  $D^*$  value of  $8.9 \times 10^8$  Jones.<sup>61</sup> These results indicate that the  $\text{MoSe}_2$ /AIGS-QDs photodetector shows promising application prospects in detecting low light intensity.

To gain a deeper comprehension of the charge transfer mechanism, ultraviolet photo-electron spectroscopy (UPS) was employed to elucidate the energy band structures of the AIGS-QDs and  $\text{MoSe}_2$ , as depicted in Fig. 4a and b. The work function ( $W_F$ ) refers to the energy of the highest occupied states and can be determined using the equation  $W_F = h\nu - E_{\text{onset}}$ ,<sup>67,68</sup> where  $h\nu = 21.21$  eV represents the energy of the incident photon and  $E_{\text{onset}}$  corresponds to the onset level associated with the secondary electrons. According to the UPS results, the work function ( $W_F$ ) values of AIGS-QDs and  $\text{MoSe}_2$  were estimated to be 3.21 eV and 4.81 eV, respectively. Subsequently, the energy of the valence band maximum ( $E_{\text{VBM}}$ ) of AIGS-QDs and  $\text{MoSe}_2$  is calculated to be 1.2 eV and 0.84 eV, respectively. Furthermore, the energy values for the conduction band minimum ( $E_{\text{CBM}}$ ) are determined to be 2.08 eV and 4.55 eV, based on the fitting of the optical bandgaps with the absorption spectrum (Fig. S8†). In conclusion, the energy band alignment diagrams of AIGS-QDs and  $\text{MoSe}_2$  (Fig. 4b) indicate that the  $\text{MoSe}_2$ /AIGS-QDs heterojunction forms a type II band alignment heterojunction.<sup>51</sup>

The increased responsivity and detectivity observed in the  $\text{MoSe}_2$ /AIGS heterojunction photodetector, as compared to the  $\text{MoSe}_2$  device, are attributed to the type II energy band alignment. When the AIGS-QDs come into contact with  $\text{MoSe}_2$  (Fig. 4c) and form a heterojunction, the difference in Fermi levels causes electrons and holes at the interface to diffuse and drift, aligning the Fermi level and establishing a new equilibrium. This results in the bending of the energy band and the formation of a depletion region, creating a built-in field.<sup>57,69</sup> Under illumination (Fig. 4d), AIGS-QDs absorb photon energy and generate electron-hole pairs. Subsequently, these pairs are efficiently separated by the inherent electric field at the



interface of the heterojunction. As a consequence, the transfer of electrons occurs towards the  $\text{MoSe}_2$  side, while holes remain on the AIGS-QDs side. As a consequence, the transfer of electron-hole pairs from AIGS-QDs to  $\text{MoSe}_2$  leads to a substantial improvement in responsivity and detectivity.<sup>67,68</sup>

To comprehensively evaluate the photoelectric performances of the  $\text{MoSe}_2$ /AIGS-QDs device, we have compared our work with similar studies and summarized the results in Table 1. The  $\text{MoSe}_2$ /AIGS-QDs device demonstrates outstanding responsivity and detectivity, highlighting its exceptional photo-response properties.

## 4. Conclusions

In summary, the sensitizing layer AIGS-QDs were successfully integrated into the  $\text{MoSe}_2$  surface to form a high-performance photodetector. The difference in the Fermi level enables the transfer of charges from AIGS-QDs to  $\text{MoSe}_2$ , resulting in a strong quenching of the PL of AIGS-QDs and a shortening in the decay time of PL in the  $\text{MoSe}_2$ /AIGS-QDs heterojunction. The photodetector with  $\text{MoSe}_2$ /AIGS-QDs heterojunction demonstrates exceptional performance attributed to its efficient charge transfer at the interface. It exhibits a responsivity of  $14.3 \text{ A W}^{-1}$  and a specific detectivity of  $6.4 \times 10^{11} \text{ Jones}$ . The responsivity and detectivity of the hybrid phototransistor are significantly enhanced by more than three times compared with that of the  $\text{MoSe}_2$  photodetector. The results present that the incorporation of AIGS-QDs sensitizing layer into  $\text{MoSe}_2$  can significantly enhance the optoelectronic performance of  $\text{MoSe}_2$  devices, making it a promising candidate for high-performance photodetector applications.

## Author contributions

XJZ and XSW contribute equally to this work. XJZ, XSW, RMJ and YHL grow the samples and fabricate the devices. XJZ, XSW, and RMJ conduct AFM, Raman, absorption spectrum and PL measurement. XJZ and YHL conduct Raman mapping and PL mapping measurement. TTG, XDH, LXW, and TZ, DNY help picture the device diagram and analysis of the XRD data. XJZ and XSW initiate the project and write the manuscript. XFS and XC provide grammar and word modification suggestions for the manuscript. XFS and XC provide suggestions and funding for the research. All authors discussed the results and approved the final version of the manuscript.

## Conflicts of interest

The authors declare no conflicts of interest.

## Acknowledgements

This work was financially supported by the National Natural Science Foundation of China (62274089, 52372152, 92064007) and the Taishan Industrial Leading Talents Project.

## References

- 1 J. Wang, F. Ma and M. Sun, *RSC Adv.*, 2017, **7**, 16801–16822.
- 2 L. Wang, Z. F. Ren, K. Y. Wang, S. J. He and L. B. Luo, *Mater. Res. Express*, 2017, **4**, 045022.
- 3 X. Hong, Y. Huang, Q. Tian, S. Zhang, C. Liu, L. Wang, K. Zhang, J. Sun, L. Liao and X. Zou, *Adv. Sci.*, 2022, **9**, 2202019.
- 4 M. K. Zhang, W. D. Liu, Y. P. Gong, Q. Liu and Z. G. Chen, *Adv. Opt. Mater.*, 2022, **10**, 2201889.
- 5 A. Pelella, A. Grillo, E. Faella, G. Luongo, M. B. Askari and A. Di Bartolomeo, *ACS Appl. Mater. Interfaces*, 2021, **13**, 47895–47903.
- 6 J. Li, C. Zhao, B. Liu, C. You, F. Chu, N. Tian, Y. Chen, S. Li, B. An, A. Cui, X. Zhang, H. Yan, D. Liu and Y. Zhang, *Appl. Surf. Sci.*, 2019, **473**, 633–640.
- 7 F. Zhang, X. Chen, Z. Zuo, X. Qin, X. Xu and X. Zhao, *J. Mater. Sci.: Mater. Electron.*, 2018, **29**, 5180–5185.
- 8 H. Zhong, L. Tang, P. Tian, L. Yu, W. Zuo and K. S. Teng, *Sensors*, 2023, **23**(4), 2254.
- 9 D. H. Kwak, P. Ramasamy, Y. S. Lee, M. H. Jeong and J. S. Lee, *ACS Appl. Mater. Interfaces*, 2019, **11**, 29041–29046.
- 10 H. J. Lee, S. Im, D. Jung, K. Kim, J. A. Chae, J. Lim, J. W. Park, D. Shin, K. Char, B. G. Jeong, J. S. Park, E. Hwang, D. C. Lee, Y. S. Park, H. J. Song, J. H. Chang and W. K. Bae, *Nat. Commun.*, 2023, **14**, 3779.
- 11 X. Song, Y. Jian, X. Wang, J. Chen, Q. Shan, S. Zhang, Z. Chen, X. Chen and H. Zeng, *Nanotechnology*, 2023, **34**, 195201.
- 12 S. Goossens, G. Navickaite, C. Monasterio, S. Gupta, J. J. Piqueras, R. Pérez, G. Burwell, I. Nikitskiy, T. Lasanta, T. Galán, E. Puma, A. Centeno, A. Pesquera, A. Zurutuza, G. Konstantatos and F. Koppens, *Nat. Photonics*, 2017, **11**, 366–371.
- 13 G. Konstantatos, M. Badioli, L. Gaudreau, J. Osmond, M. Bernechea, F. P. G. de Arquer, F. Gatti and F. H. L. Koppens, *Nat. Nanotechnol.*, 2012, **7**, 363–368.
- 14 Z. T. Hu, T. Gan, L. Du, J. Z. Zhang, H. Xu, S. L. Han, H. L. Xu, F. Liu, Y. P. Chen and G. Chen, *J. Infrared, Millimeter, Terahertz Waves*, 2019, **38**, 269–274.
- 15 J. J. Zheng, Y. R. Wang, K. H. Yu, X. X. Xu, X. X. Sheng, E. T. Hu and W. Wei, *Acta Phys. Sin.*, 2018, **67**, 118502.
- 16 F. X. Liang, Y. Gao, C. Xie, X. W. Tong, Z. J. Li and L. B. Luo, *J. Mater. Chem. C*, 2018, **6**, 3815–3833.
- 17 H. Yao, X. Guo, A. Bao, H. Mao, Y. Ma and X. Li, *Chin. Phys. B*, 2022, **31**, 038501.
- 18 M. Ye, D. Zhang and Y. K. Yap, *Electronics*, 2017, **6**, 43.
- 19 W. Choi, N. Choudhary, G. H. Han, J. Park, D. Akinwande and Y. H. Lee, *Mater. Today*, 2017, **20**, 116–130.
- 20 P. V. Pham, S. C. Bodepudi, K. Shehzad, Y. Liu, Y. Xu, B. Yu and X. Duan, *Chem. Rev.*, 2022, **122**, 6514–6613.
- 21 Z. Zhu, I. Murtaza, H. Meng and W. Huang, *RSC Adv.*, 2017, **7**, 17387–17397.
- 22 D. M. Geum, S. Kim, J. Khym, J. Lim, S. Kim, S. Y. Ahn, T. S. Kim, K. Kang and S. Kim, *Small*, 2021, **17**, 2007357.
- 23 C. Song, G. Noh, T. S. Kim, M. Kang, H. Song, A. Ham, M. kyung Jo, S. Cho, H. J. Chai, S. R. Cho, K. Cho, J. Park, S. Song, I. Song, S. Bang, J. Y. Kwak and K. Kang, *ACS Nano*, 2020, **14**, 16266–16300.
- 24 H. S. Nalwa, *RSC Adv.*, 2020, **10**, 30529–30602.



25 H. Li, K. Zhang, X. Li, B. Liu, L. Li, Z. Mei, T. Chen, Q. Liu, W. Yu, J. Yuan, H. Mu and S. Lin, *Mater. Des.*, 2023, **227**, 111799.

26 A. Grillo, Z. Peng, A. Pelella, A. Di Bartolomeo and C. Casiraghi, *ACS Nano*, 2023, **17**, 1533–1540.

27 S. Zhang, X. Wang, Y. Chen, G. Wu, Y. Tang, L. Zhu, H. Wang, W. Jiang, L. Sun, T. Lin, H. Shen, W. Hu, J. Ge, J. Wang, X. Meng and J. Chu, *ACS Appl. Mater. Interfaces*, 2019, **11**, 23667–23672.

28 C. Hu, D. Dong, X. Yang, K. Qiao, D. Yang, H. Deng, S. Yuan, J. Khan, Y. Lan, H. Song and J. Tang, *Adv. Funct. Mater.*, 2017, **27**, 1603605.

29 S. Mukherjee, S. Jana, T. K. Sinha, S. Das and S. K. Ray, *Nanoscale Adv.*, 2019, **1**, 3279–3287.

30 L. Yu, P. Tian, L. Tang, W. Zuo, H. Zhong, Q. Hao, K. S. Teng, G. Zhao, R. Su, X. Gong and J. Yuan, *Sensors*, 2023, **23**(9), 4328.

31 M. M. Ackerman, X. Tang and P. Guyot Sionnest, *ACS Nano*, 2018, **12**, 7264–7271.

32 H. Kan, S. Liu, B. Xie, B. Zhang and S. Jiang, *J. Mater. Sci.: Mater. Electron.*, 2017, **28**, 9782–9787.

33 Z. Hu, H. Lu, W. Zhou, J. Wei, H. Dai, H. Liu, Z. Xiong, F. Xie, W. Zhang and R. Guo, *J. Mater. Sci. Technol. Res.*, 2023, **134**, 189–196.

34 W. Hoisang, T. Uematsu, T. Torimoto and S. Kuwabata, *Nanoscale Adv.*, 2022, **4**, 849–857.

35 G. Huang, Y. Huang, Z. Liu, J. Wei, Q. Zhu, G. Jiang, X. Jin, Q. Li and F. Li, *J. Lumin.*, 2021, **233**, 117903.

36 J. H. Kim, B. Y. Kim, E. P. Jang, S. Y. Yoon, K. H. Kim, Y. R. Do and H. Yang, *Chem. Eng. J.*, 2018, **347**, 791–797.

37 G. Huang, Y. Huang, Z. Liu, J. Wei, Q. Zhu, G. Jiang, X. Jin, Q. Li and F. Li, *J. Lumin.*, 2021, **233**, 117903.

38 H. J. Lee, S. Im, D. Jung, K. Kim, J. A. Chae, J. Lim, J. W. Park, D. Shin, K. Char, B. G. Jeong, J. S. Park, E. Hwang, D. C. Lee, Y. S. Park, H. J. Song, J. H. Chang and W. K. Bae, *Nat. Commun.*, 2023, **14**, 3779.

39 W. Hoisang, T. Uematsu, T. Torimoto and S. Kuwabata, *Inorg. Chem.*, 2021, **60**, 13101–13109.

40 W. Du, P. Yu, J. Zhu, C. Li, H. Xu, J. Zou, C. Wu, Q. Wen, H. Ji, T. Liu, Y. Li, G. Zou, J. Wu and Z. M. Wang, *Nanotechnology*, 2020, **31**, 225201.

41 A. Bala, B. So, P. Pujar, C. Moon and S. Kim, *ACS Nano*, 2023, **17**, 4296–4305.

42 W. A. Abdallah and A. E. Nelson, *J. Mater. Sci.*, 2005, **40**, 2679–2681.

43 X. Zhao, J. Sui, F. Li, H. Fang, H. Wang, J. Li, W. Cai and G. Cao, *Nanoscale*, 2016, **8**, 17902–17910.

44 S. Y. Chen, C. Zheng, M. S. Fuhrer and J. Yan, *Nano Lett.*, 2015, **15**, 2526–2532.

45 P. Tonndorf, R. Schmidt, P. Böttger, X. Zhang, J. Börner, A. Liebig, M. Albrecht, C. Kloc, O. Gordan, D. R. T. Zahn, S. Michaelis de Vasconcellos and R. Bratschitsch, *Opt. Express*, 2013, **21**, 4908–4916.

46 X. Wang, D. Yan, C. Zhu, Y. Feng, T. Guo, R. Jia, K. Qu, L. Li, T. Zhao, Y. Xiong, A. Farhan, Y. Lin, L. Wu, Y. Dong, S. Zhang, X. Chen and X. Song, *2D Mater.*, 2023, **10**, 045020.

47 M. Peng, X. Xie, H. Zheng, Y. Wang, Q. Zhuo, G. Yuan, W. Ma, M. Shao, Z. Wen and X. Sun, *ACS Appl. Mater. Interfaces*, 2018, **10**, 43887–43895.

48 Q. Zhang, F. Yang, S. Zhou, N. Bao, Z. Xu, M. Chaker and D. Ma, *Appl. Catal., B*, 2020, **270**, 118879.

49 A. Bora, S. Paul, M. T. Hossain and P. K. Giri, *J. Phys. Chem. C*, 2022, **126**, 12623–12634.

50 M. T. Hossain, L. P. L. Mawlong, T. Jena, A. Bora, U. Nath, M. Sarma and P. K. Giri, *ACS Appl. Nano Mater.*, 2023, **6**, 11023–11036.

51 H. Wu, Z. Kang, Z. Zhang, Z. Zhang, H. Si, Q. Liao, S. Zhang, J. Wu, X. Zhang and Y. Zhang, *Adv. Funct. Mater.*, 2018, **28**, 1802015.

52 T. Shen, F. Li, Z. Zhang, L. Xu and J. Qi, *ACS Appl. Mater. Interfaces*, 2020, **12**, 54927–54935.

53 J. Qiao, F. Feng, S. Song, T. Wang, M. Shen, G. Zhang, X. Yuan and M. G. Somekh, *Adv. Funct. Mater.*, 2022, **32**, 2110706.

54 J. K. Qin, D. D. Ren, W. Z. Shao, Y. Li, P. Miao, Z. Y. Sun, P. Hu, L. Zhen and C. Y. Xu, *ACS Appl. Mater. Interfaces*, 2017, **9**, 39456–39463.

55 A. Xie, Y. Jian, Z. Cheng, Y. Gu, Z. Chen, X. Song and Z. Yang, *J. Phys.: Condens. Matter*, 2022, **34**, 154007.

56 H. Meng, F. Zhang, Z. Mo, Q. Xia, M. Zhong and J. He, *J. Phys. D*, 2022, **55**, 444006.

57 Y. H. Zhou, Z. B. Zhang, P. Xu, H. Zhang and B. Wang, *Nanoscale Res. Lett.*, 2019, **14**, 364.

58 S. Qin, K. Li, J. Zhu, H. Xu, N. Ali, A. Rahimi-Iman and H. Wu, *J. Alloys Compd.*, 2021, **856**, 158179.

59 R. Ghosh, Y. S. Kang, K. Yadav, H. Lin, Z. L. Yen, H. Y. Lin, G. Z. Lu, R. Sankar, Y.-P. Hsieh, M. Hofmann and Y. F. Chen, *ACS Appl. Electron. Mater.*, 2022, **4**, 5208–5214.

60 S. Pak, Y. Cho, J. Hong, J. Lee, S. Lee, B. Hou, G. H. An, Y.-W. Lee, J. E. Jang, H. Im, S. M. Morris, J. I. Sohn, S. Cha and J. M. Kim, *ACS Appl. Mater. Interfaces*, 2018, **10**, 38264–38271.

61 S. Mukherjee, D. Bhattacharya, S. Patra, S. Paul, R. K. Mitra, P. Mahadevan, A. N. Pal and S. K. Ray, *ACS Appl. Mater. Interfaces*, 2022, **14**, 5775–5784.

62 S. Lee, J. Y. Kim, S. Choi, Y. Lee, K. S. Lee, J. Kim and J. Joo, *ACS Appl. Mater. Interfaces*, 2020, **12**, 25159–25167.

63 Md. S. Hassan, S. Bera, D. Gupta, S. K. Ray and S. Sapra, *ACS Appl. Mater. Interfaces*, 2019, **11**, 4074–4083.

64 P. J. Ko, A. Abderrahmane, N. H. Kim and A. Sandhu, *Semicond. Sci. Technol.*, 2017, **32**, 065015.

65 B. Kundu, O. Özdemir, M. Dalmases, G. Kumar and G. Konstantatos, *Adv. Opt. Mater.*, 2021, **9**, 2101378.

66 S. Kim, D. Lee, S. Moon, J. Choi, D. Kim, J. Kim and S. Baek, *Adv. Funct. Mater.*, 2023, **33**, 2303778.

67 Y. Pak, S. Mitra, N. Alaal, B. Xin, S. Lopatin, D. Almalawi, J.-W. Min, H. Kim, W. Kim, G. Y. Jung and I. S. Roqan, *Appl. Phys. Lett.*, 2020, **116**, 112102.

68 H. Wu, H. Si, Z. Zhang, Z. Kang, P. Wu, L. Zhou, S. Zhang, Z. Zhang, Q. Liao and Y. Zhang, *Adv. Sci.*, 2018, **5**, 1801219.

69 Y. Wu, S. E. Wu, J. Hei, L. Zeng, P. Lin, Z. Shi, Q. Chen, X. Li, X. Yu and D. Wu, *Nano Res.*, 2023, **16**, 11422–11429.

